Single-cell atlas of a non-human primate reveals new pathogenic mechanisms of COVID-19

Lei Han,[1,2,15] Xiaoyu Wei,[1,2,3,15] Chuanyu Liu,[1,2,14,15] Giacomo Volpe,[4,15] Zhifeng Wang,[1,2,15] Taotao Pan,[1,2,3] Yue Yuan,[1,2,3] Ying Lei,[1,2,14] Yiwei Lai,[4] Carl Ward,[4] Yeya Yu,[1,2,5] Mingyue Wang,[1,2,3] Quan Shi,[1,2,6] Tao Wu,[1,2] Liang Wu,[1,2,3] Ya Liu,[1,2] Chunqing Wang,[1,2,3] Yuanhang Zhang,[1,2,3] Haixi Sun,[1,2] Hao Yu,[1,2] Zhenkun Zhuang,[1,2,7] Tingting Tang,[1,2] Yunting Huang,[2] Haorong Lu,[2] Liqin Xu,[1,2,6] Jiangshan Xu,[1,2,3] Mengnan Cheng,[1,2,3] Yang Liu,[1,2,3] Chi Wai Wong,[8] Tao Tan,[9] Weizhi Ji,[9] Patrick H. Maxwell,[12] Huanming Yang,[1,10] Jian Wang,[1,10] Shida Zhu,[1,2] Shiping Liu,[1,2,13] Xun Xu,[1,2,11,*] Yong Hou,[1,2,13,*] Miguel A. Esteban,[4,16,*] and Longqi Liu[1,2,14,*]

[1]BGI-Shenzhen, Shenzhen 518083, China

[2]China National GeneBank, BGI-Shenzhen, Shenzhen 518120, China

[3]BGI Education Center, University of Chinese Academy of Sciences (CAS), Shenzhen 518083, China

[4]Laboratory of Integrative biology, Guangzhou Institutes of Biomedicine and Health, CAS, Guangzhou 510530, China

[5]BGI College, Zhengzhou University, Zhengzhou 450000, China

[6]Laboratory of Genomics and Molecular Biomedicine, Department of Biology, University of Copenhagen, Copenhagen 2200, Denmark

[7]School of Biology and Biological Engineering, South China University of Technology, Guangzhou 510006, China

[8]Huazhen Biosciences, Guangzhou 510900, China

[9]Yunnan Key Laboratory of Primate Biomedical Research, Institute of Primate Translational Medicine, Kunming University of Science and Technology, Kunming 650500, China

[10]James D. Watson Institute of Genome Science, Hangzhou, 310008, China

[11]Institute for Stem Cells and Regeneration, CAS, Beijing 100101, China

[12]Cambridge Institute for Medical Research, Department of Medicine, University of Cambridge, Cambridge CB2 0XY, United Kingdom

[13]Shenzhen Key Laboratory of Single-Cell Omics, BGI-Shenzhen, Shenzhen 518120, China

[14]Shenzhen Bay Laboratory, Shenzhen 51800, China

32   [15]These authors contributed equally

33   [16]Lead Contact

34

35   *Correspondence: xuxun@genomics.cn   (X.X.),   houyong@genomics.cn   (Y.H.),

36   miguel@gibh.ac.cn (M.A.E.), liulongqi@genomics.cn (L.L.)

37

38   **Key words:**

39   Single-cell transcriptome, non-human primate, COVID-19, SARS-CoV-2, ACE2, TMPRSS2,

40   Interleukin 6, STAT transcription factors, immune cell exhaustion

41

42   **Bullet points:**

43   1-We used a single-cell transcriptome atlas of 9 monkey tissues to study COVID-19.

44   2-*ACE2*$^+$*TMPRSS2*$^+$ epithelial cells of lung, kidney and liver are targets for SARS-CoV-2.

45   3-*ACE2* correlation analysis shows *IDO2* and *ANPEP* as potential therapeutic opportunities.

46   4-We unveil a link between IL6, STAT transcription factors and boosted SARS-CoV-2 entry.

47

48

49   **ABSTRACT**

50

51   Stopping COVID-19 is a priority worldwide. Understanding which cell types are targeted by

52   SARS-CoV-2 virus, whether interspecies differences exist, and how variations in cell state

53   influence viral entry is fundamental for accelerating therapeutic and preventative

54   approaches. In this endeavor, we profiled the transcriptome at single-cell resolution of nine

55   tissues from a Macaca fascicularis monkey. The distribution of SARS-CoV-2 facilitators, ACE2

56   and TMRPSS2, in different cell subtypes showed substantial heterogeneity across lung,

57   kidney, thyroid and liver. Co-expression analysis identified immunomodulatory proteins such

58   as IDO2 and ANPEP as potential SARS-CoV-2 targets responsible for immune cell exhaustion.

59   Furthermore, single-cell chromatin accessibility analysis of the kidney unveiled a plausible link

60   between IL6-mediated innate immune responses aiming to protect tissue and enhanced ACE2

61   expression that could promote viral entry. Our work constitutes a unique resource for

62   understanding SARS-CoV-2 pathophysiology in two phylogenetically close species, which

63   might guide in the development of effective treatments in humans.

64

INTRODUCTION

As the distance between humans and wild animal habitats diminishes due to uncontrolled human expansion, a series of zoonotic diseases with high mortality rates have emerged. For instance, the recent outbreak of Ebola in Africa, which killed over 5,000 people, was most likely spread from bats and primates to humans (Kock et al., 2019). The current outbreak of coronavirus disease 2019 (COVID-19) caused by the coronavirus severe acute respiratory syndrome coronavirus 2 (SARS-CoV-2) (Zhu et al., 2020) is not the only example of coronaviruses that have recently passed from animals to humans. Coronaviruses are a family of RNA viruses that typically cause respiratory tract infections in humans, yet they are frequently in the reservoir of wild animals with no disease (Cui et al., 2019). For example, the common cold is often (10-15%) caused by a coronavirus (e.g. HCoV-229E and HCoV-OC43) (Su et al., 2016). However, coronaviruses can also lead to severe and life-threatening diseases. In the early 2000s a coronavirus called SARS-CoV, believed to be passed from bats to humans in South East Asia, caused more than 700 deaths from around 8,000 confirmed cases worldwide (Lau et al., 2005). Since 2012, another zoonotic coronavirus which is believed to have passed from camels to humans in the Middle East was designated as Middle East Respiratory Syndrome (MERS) (Reusken et al., 2013). To date, there have been over 2,500 confirmed cases of MERS with over 800 deaths. While SARS appears to have been eradicated, MERS cases are sporadic and human to human spread is limited (Su et al., 2016).

As of 2nd April 2020, COVID-19 (Zhu et al., 2020) has become a global pandemic with more than 930,000 confirmed cases and over 47,000 deaths. Due to its high infectivity rate and the high level of intensive care that many patients need, COVID-19 has overwhelmed national health services and destabilized the world. One important reason is that many people who are positive for the virus show mild symptoms (Chan et al., 2020; Rothe et al., 2020), leading to unnoticed spread of the virus. The current worldwide emergency, possibility of expansion to less developed countries, risk of virus mutations and the perpetuation beyond this season has made it imperative to stop the current trajectory of virus spreading. Developing drugs and preventative vaccines are ongoing but to warrant success it is necessary to have more knowledge about the disease mechanisms. So far, little is known except for the viral binding via angiotensin converting enzyme 2 (ACE2) and subsequent priming by type 2 transmembrane serine protease 2 (TMPRSS2) protease, which are shared mechanisms with

97   SARS and MERS (Hoffmann et al., 2020; Walls et al., 2020). To test experimental treatments,

98   animal models close to humans are necessary due to sequence variation of ACE2 and changes

99   in the proportions of cell subtypes in organs between species. For these reasons, it is essential

100   to have a species close to human to study COVID-19. In this regard, monkey experiments have

101   already shown that reinfection of SARS-CoV-2 is preventable by acquired immunity, thus,

102   largely debunking one of the initial myths about the disease (Bao et al., 2020).

103   Questions about the proportions of cell types within organs between species and their

104   crosstalk can be addressed effectively through single-cell profiling technologies, in particular

105   single-cell RNA sequencing (RNA-seq) and single-cell assay for transposase accessible

106   chromatin sequencing (ATAC-seq). Yet, although human data are accumulating (Han et al.,

107   2020), monkey data are still scarce. The comparison between human and monkey data will

108   be crucial for advancing our knowledge of COVID-19.

109   Here, we provide a high-resolution single-cell atlas of nine organs/tissues (lung, kidney,

110   pancreas, brain, parotid, liver, thyroid, aorta artery, and blood) in monkey, encompassing

111   215,334 cells. By comparing the expression of SARS related targets in monkey and human, we

112   have identified cell-to-cell similarities as expected. Crucially, we also discovered stark

113   differences in *ACE2* expression between these two species, for example in the ciliated vs

114   alveolar type 2 cells of the lung and the hepatocytes in liver. We also observed that *ACE2* is

115   heterogeneous among different epithelial cell subtypes across these organs/tissues,

116   suggesting that variations in cell state could influence viral entry. Supporting this, single-cell

117   ATAC-seq of monkey kidney identified regulatory elements driven by STAT transcription

118   factors and interferon regulatory factor (IRF) in the *ACE2* locus. This suggests that cytokines,

119   particularly IL6, aiming to induce a tissue protective response can exacerbate the disease by

120   aiding viral entry into target cells. Additionally, through correlation analysis with *ACE2*

121   expression, we have identified several potential candidates involved in COVID-19

122   pathophysiology, such as Transmembrane protein 27 (TMEM27), Indoleamine 2,3-

123   dioxygenase 2 (IDO2), DnaJ heat shock protein family (Hsp40) member C12 (DNAJC12) and

124   Alanyl aminopeptidase N (ANPEP). These targets may offer therapeutic opportunities.

125   Taken together, our data constitute a unique resource which will aid the scientific community

126   in the fight against SARS-CoV-2. From a wider perspective, this will also be useful for

127   comparative studies aimed at understanding physiological differences between monkey and

128   other species, in particular, human.

RESULTS

Cellular heterogeneity of nine non-human primate tissues assessed by single-cell RNA-seq

We profiled, at the single-cell level, the transcriptome of the model organism cynomolgus monkey *(Macaca fascicularis)*, as it is phylogenetically close to human and this could help advance our knowledge of human physiology and disease. As proof of principle, we decided to use our data to understand how SARS-CoV-2 spreads and triggers the clinical features that have been lethal in a number of patients. For this study, we used a six-year-old female monkey in which we profiled nine different organs (indicated in **Fig. 1A**). These included lung, liver and kidney as the known affected organs by the closely related SARS-CoV infection (Hamming et al., 2004), and have been reported to have high *ACE2* expression in human (Naicker et al., 2020). Peripheral blood mononuclear cells (PBMC) were added because altered immune responses are thought to be detrimental in the disease (Conti et al., 2020). Neocortex was chosen because of the clinical symptoms which involve loss of smell and taste suggesting that the central nervous system may be targeted (Bagheri et al., 2020). The parotid gland was chosen on the basis that saliva is one of the main means of infection spread. Additionally, we selected aorta, thyroid and pancreas.

We employed a high-throughput platform recently developed in-house, DNBelab C4, which is a scalable and cost-effective approach for microfluidic droplet-based approach (Liu et al., 2019). Except for PBMC sequencing, which was performed using cells in suspension, the sequencing for all the other organs was done using single-nucleus library preparations. Following euthanasia, the selected organs were extracted, single-nucleus/cell suspensions were obtained and used for library preparation. A total of 40,226 liver, 45,286 kidney, 36,421 pancreas, 44,355 parotid gland, 12,822 lung, 7,877 thyroid, 6,361 neocortex, 2,260 aorta and 19,726 nuclei/PBMC passed quality control and were used for downstream analysis (**Supplemental table 1, Fig. S1A, B**).

In a global view of our single-cell dataset, each organ clustered separately, with the exception of a few cell types such as macrophages, adipocytes and endothelial cells, which were shared between different organs (**Fig. 1B**). We performed Uniform Manifold Approximation and Projection (UMAP) on the 215,334 cells and identified 44 major clusters by performing unbiased graph-based Louvain clustering (**Supplemental table 1**). Some clusters were largely composed of cells belonging to a specific tissue, such as hepatocytes in cluster 14, pancreas

161   acinar cells in cluster 27 and parotid acinar cells in cluster 31 (**Fig. 1C, S1C**). We next

162   performed clustering and differential gene expression analysis to dissect the cellular

163   composition of each individual organ. This analysis confirmed the typical patterns of cell

164   heterogeneity for all the organs/tissues. When examining the lung tissue, we defined 10

165   major clusters with specific molecular markers, including ciliated cells, macrophages,

166   fibroblasts, pericytes, alveolar (pneumocytes) type 1 and type 2, endothelial and club cells

167   (**Fig. S2A**). The kidney consisted of 11 clusters, those being podocytes, thick ascending limb

168   cell, proximal tubule cells, intercalated cells 1 and 2, connecting tubule cells, distal convoluted

169   tubule cells, stomal cells, thin limb cells, principal cells and endothelial cells (**Fig. S2B**). Analysis

170   of liver tissue revealed hepatocytes to be the larger population of cells, while other clusters

171   consisted of cholangiocytes, macrophages (Kupffer cells), natural killer-T (NK-T) cells,

172   endothelial cells and hepatic stellate cells (**Fig. S2C**). In agreement with previous data,

173   inspection of PBMC clustering revealed large populations of B cells, $CD4^+$, $CD8^+$ naïve and $CD8^+$

174   memory T cells, together with smaller populations of natural killer (NK) cells, dendritic cells,

175    $CD16^+$ and $CD14^+$ monocytes (**Fig. S2D**). We clustered the neocortex and found excitatory

176   neurons, astrocytes, microglia, parvalbumin (PVALB), somatostatin-expressing neurons (SST),

177   synaptic vesicle glycoprotein-expressing cells (SV2C), vasoactive intestinal polypeptide-

178   expressing neurons (VIP), oligodendrocytes and oligodendrocyte precursor cells (**Fig S2E**).

179   Parotid gland instead was composed of a large cluster of serous acinar cells together with

180   small clusters of macrophages, myoepithelial cells, striated duct cells, mucous acinar cells and

181   intercalated duct cells (**Fig. S2F**). Aorta cells could be further divided into adipocytes,

182   endothelial cells, myofibroblasts and a large proportion of smooth muscle cells (**Fig. S2G**). Our

183   clustering also demonstrated that most of the thyroid gland is composed of follicular cells,

184   with smaller populations of adipocytes, endothelial cells, stromal and smooth muscle cells

185   (**Fig. S2H**). Finally, our data showed the largest population of the pancreas to be acinar cells,

186   while smaller clusters were comprised of macrophages, ductal, alpha and beta cells (**Fig. S2I**).

187   In conclusion, we have successfully profiled the transcriptome of nine organs at a single-cell

188   resolution in monkey, which could assist in the study of COVID-19.

189

190   ***ACE2* and *TMPRSS2* single-cell expression landscape in a non-human primate**

191   Recent studies have reported that, similarly to SARS-CoV, the capacity of SARS-CoV-2 virus to

192   infect host cells relies on viral spike (S) protein binding to ACE2 entry receptor (Hoffmann et

193 al., 2020; Walls et al., 2020), which is involved in the control of blood pressure through the

194 renin-angiotensin system (Turner et al., 2004). This phenomenon is primed by the

195 multifunction serine protease TMPRSS2 (Kim et al., 2006). Accordingly, double positive

196 (ACE2$^+$/TMPRSS2$^+$) cells have a higher risk of infection by SARS-CoV-2. Although

197 immunohistological studies have demonstrated localization of these two proteins in the

198 respiratory tract (Jia et al., 2005), it is unclear how many cell subtypes express these genes

199 and how homogenous the expression among a specific cell subtype is. Also, comprehensive

200 information about other cell types and organs that express these two proteins and could be

201 targeted by the virus in human or monkey is lacking.

202 We inspected our data to see how widespread and homogenous *ACE2* expression was in the

203 monkey tissues. As expected, *ACE2* was detected in several lung clusters, such as ciliated cells,

204 club cells and pulmonary alveolar type 2 cells (**Fig. 2A, 3A upper panel**). In the kidney, *ACE2*

205 was primarily present in proximal tubule cells, though interestingly, the expression was

206 heterogenous (**Fig. 2A, 3B upper panel**). This is consistent with reports that a significant

207 number of COVID-19 patients display altered kidney function (Li et al., 2020; Naicker et al.,

208 2020). In the liver, *ACE2* was mostly expressed in cholangiocytes, with a smaller degree of

209 expression also found in hepatocytes (**Fig. 2A, 3C upper panel**). Notably, the closely related

210 SARS-CoV caused liver injury due to hepatitis in some patients (Peiris et al., 2003), suggesting

211 that the liver may also be a direct target for SARS-CoV-2. Likewise, ACE2 was detected in

212 follicular cells within the thyroid tissue (**Fig. S3**). In contrast, little or no expression was

213 observed in neocortex, pancreas, parotid and PBMC (**Fig. 2A, S3A**).

214 On the other hand, *TMPRSS2* displayed widespread expression across multiple tissues,

215 although it was highest in kidney cells. However, in contrast to *ACE2*, its expression was

216 highest in the distal convoluted tubule, thin limb, intercalated and principal cell 1 and 2 kidney

217 clusters (**Fig. 2B, 3B lower panel, S3B**). Additionally, significant *TMPRSS2* was observed in

218 both parotid and pancreatic acinar cells, follicular cells and in several lung clusters (**Fig. 2B**).

219 We then determined which cells co-expressed both genes (*ACE2*$^+$/*TMPRSS2*$^+$). The largest

220 overlap was observed in the ciliated and club cell clusters of the lung and the proximal tubule

221 cells of the kidney. A smaller overlap was observed in hepatocytes and pancreatic cells (**Fig.**

222 **2C, 2E, 3A lower panel, 3C lower panel**).

223 Therefore, our data show that *ACE2* and *TMPRSS2* are expressed in a variety of cell types,

224 mainly epithelial cells, within the nine monkey organs/tissues (**Supplemental table 2A**). They

also suggest that variations in cell state (e.g. differentiation state, stimulation state or topographical distribution) cause heterogenous expression across an individual tissue. These observations may provide important clues about COVID-19 pathogenesis and symptomatology.

Comparative analysis of *ACE2* and *TMPRSS2* expression in human and non-human primate

Given the heterogeneous nature of *ACE2* and *TMPRSS2* expression in monkey tissues, we decided to investigate similarities and differences between human and monkey. For this purpose, we retrieved publicly available data from single-cell studies in human (see methods). *TMPRSS2* distribution was similar in cell subtypes of lung, kidney and liver between human and monkey (**Fig. 3D-3F**). However, strikingly, *ACE2* showed distinct patterns among cell subtypes in all three organs between the two species (**Fig. 3D-3F**). The biggest differences were observed in ciliated cells of the lung, which had the highest expression of *ACE2* in monkey, and pulmonary alveolar type 2 cells, which had the highest expression of *ACE2* in human. The function of ciliated cells is to move substances (e.g. cell debris and toxic material) across the surface of the respiratory tract and are commonly targeted by respiratory viruses, whereas pulmonary alveolar type 2 cells have regenerative properties, are crucial for alveolar homeostasis and produce surfactant (Hamm et al., 1992; Mason and Williams, 1977). In the kidney of both monkey and human, the highest *ACE2* expression was in proximal tubule cells (**Fig. 3E**), which are responsible for electrolyte and nutrient reabsorption. However, renal endothelial cells had higher expression in monkey compared to human. In liver, cholangiocytes had similarly high *ACE2* expression in monkey and human, but hepatocytes showed higher expression and more positive cells in the human (**Fig. 3F**). After discovering heterogenous expression of *ACE2* within the proximal tubule cells, we revisited the previously analyzed data and were able to sub cluster this population of cells into two (S1 and S3) based on the expression of *SLC5A2* and *SLC7A13* (Lee et al., 2015) (**Supplemental table 2B, Fig. S4**). These two genes are sodium and glucose cotransporters involved in glucose reabsorption in the kidney (Santer and Calado, 2010; Yu et al., 2011). We did not include thyroid, pancreas or aorta in these analyses because of lack of high-quality available human single-cell datasets. As for the neocortex and PBMC, they have little to no expression of *ACE2* in human (data not shown).

256   These differences in *ACE2* expression across cell subtypes in the lung, kidney and liver in

257   monkey and human raise the possibility that infection with SARS-CoV-2 in the two species will

258   have different effects.

259

260   ***ACE2* correlation analysis across cell types reveals potentially therapeutic targets**

261   To shed light on potential mechanisms that could facilitate *ACE2*-mediated SARS-CoV-2

262   infection, we performed an analysis of the Pearson's correlation coefficient, based on gene

263   expression in the 44 cell subtypes, to determine what genes are co-regulated with *ACE2* in

264   monkey tissues. Correlated genes were considered as those displaying a coefficient higher

265   than 0.6 with an adjusted p-value < 0.001. Using these criteria, we observed several genes

266   with marked correlation, including genes that belong to metabolic and developmental

267   pathways and genes involved in the cellular response to xenobiotic stimuli (**Fig. 4A, B**). The

268   highest correlation was observed for transmembrane protein 27 (*TMEM27*, cor = 0.84), a

269   protein involved in trafficking amino acid transporters to the apical brush border of kidney

270   proximal tubules (Chu et al., 2017). This is unsurprising considering that *TMEM27* is an

271   important paralog of *ACE2*, and high expression was restricted to kidney cells. DnaJ heat shock

272   protein family (Hsp40) member C12 (*DNAJC12*, cor = 0.78), a gene with a role in immune

273   response processes (Sigdel et al., 2013), had a distribution like *TMEM27*. Importantly, we also

274   observed high correlation with Indoleamine 2,3-dioxygenase 2 (*IDO2*, cor = 0.77), a gene with

275   abundant expression in kidney and liver cells that was also expressed in the lung and other

276   organs. *IDO2* has been shown to function during the early phases of immune responses and

277   to mediate inflammatory autoimmunity (Ball et al., 2009; Lepiller et al., 2015). *ANPEP*, which

278   encodes for alanyl aminopeptidase N, was also co-expressed with *ACE2* in kidney, liver and to

279   a lesser extent in lung too (cor = 0.64), like *IDO2* (**Fig. 4C, D**). Interestingly, *ANPEP* has also

280   been shown to be participate in immune responses, virus receptor activity and in mediating

281   virus entry into host cells (Delmas et al., 1992; Wentworth and Holmes, 2001).

282   These data highlight potential therapeutic targets to help in the fight against SARS-CoV-2. Due

283   to their potential co-regulation with ACE2, DNAJC12 and ANPEP it is possible that they

284   modulate, or are directly involved in viral entry. Alternatively, depletion of cells expressing

285   *IDO2* and *ANPEP,* through a cytopathic effect of the virus, could trigger an uncontrolled

286   immune response and contribute to the immune cell exhaustion observed in COVID-19 (Guo

287   et al., 2020).

Epigenetic regulation of *ACE2* in each cell subtype of the monkey kidney

To understand whether epigenetic mechanisms underlie the heterogeneity of cellular composition and cell state variation in the kidney, we employed DNBelab C4 technology to perform high-throughput single-cell ATAC-seq (**Fig. 5A**). After filtering, 6,353 nuclei were used for downstream analysis (**Supplemental table 4, Fig. S5A, B**). We integrated these data with the kidney transcriptomic data described in **Fig. 1** and proceeded to perform Louvain clustering to map all the different cell types within the dataset (**Fig. 5B**). Consistent with the transcriptomic data, our epigenomic mapping identified thick ascending limb cells and proximal tubule cells as the largest kidney clusters (**Fig. S2B**). Similarly, smaller clusters of podocytes, principal, intercalated, connected tubule, distal convoluted tubule, thin limb, endothelial and stromal cells were detected (**Fig. 5C, S5C**). Analysis of open chromatin regions revealed discrete peaks in the *ACE2* locus, with the highest signal detected in proximal tubule cells S1 and S3, which are also the highest *ACE2*-expressing cells (**Fig. 5D**). Our approach failed to detect significant signal enrichment in the *ACE2* locus in endothelial cells, possibly related to the low level of expression (**Fig. 5D**). Within the cells of the kidney we observed the highest percentage of *ACE2*$^+$ cells in the proximal tubule S3, with a lower percentage in the proximal tubule S1 and endothelial cells (**Fig. 5E**). Motif analysis within the open chromatin regions in *ACE2*$^+$ cells demonstrated that these regions were preferentially enriched in signal transducer and activator of transcription 1 and 3 (STAT1 and 3) and interferon regulatory factor 1 (IRF1) binding sites (**Fig. 5F**). These findings suggested that tissue protective cytokines including IL5, IL6, EGF and interferons are acting on these proximal tubule cells S3 to induce *ACE2*. We focused on IL6 because a recent clinical trial has been started that uses anti-IL6 receptor (IL6R) antibodies in the treatment of COVID-19 (http://www.chictr.org.cn/showprojen.aspx?proj=49409). IL6 is a potent regulator of immune responses and can be produced by a variety of interstitial cells including fibroblasts, endothelial cells and more importantly tissue macrophages (Heinrich et al., 1990). Interestingly, we also noticed that distribution of *IL6R* correlated well with *ACE2* in proximal tubule cells (**Fig. 5G, Supplemental Fig. S5D**). In human kidney a similar co-expression pattern was detected (**Fig. 5H**).

Our observations suggest a potential positive feedback loop between IL6 and ACE2 expression that can exacerbate COVID-19 disease progression due to increased viral entry and dissemination.

DISCUSSION

Mammalian tissues and organs are composed of many different cell types that can vary in abundance and cell state. Tissue heterogeneity is only beginning to be unraveled thanks to the advent of single-cell profiling technologies that allow us to precisely map transcriptomic and epigenomic programs. These technologies are revolutionizing our view of human physiology and disease. Great efforts are being made to generate the first version of both human and murine atlases (Han et al., 2018; Han et al., 2020); the mouse is among the most commonly used model organisms in biomedical research, but many developmental or pathological aspects are not paralleled in human. Understanding tissue and organ complexity in species that are phylogenetically close to humans is an unmet requirement.

In this study, we have generated a single-cell transcriptomic atlas of nine organs (liver, kidney, lung, pancreas, neocortex, aorta, parotic gland, thyroid and peripheral blood) from cynomolgus monkey. We used this dataset not only to provide fundamental information about the cellular composition of the different tissues tested but also as a platform to dissect the overall expression distribution of the SARS-CoV-2 entry receptor, ACE2, and its serine protease coactivator TMPRSS2 (Hoffmann et al., 2020; Walls et al., 2020). Interestingly, ACE2 was expressed in multiple epithelial tissues besides the lung, specifically the kidney, liver and thyroid. Other organs of epithelial origin such as the gut have also been implicated in the pathogenesis of the disease (Ong et al., 2020). A consequence of this is that the SARS2-CoV-2 virus could infect these organs too, which would explain some of the reported clinical manifestations of COVID-19 (Zhu et al., 2020). By comparing our dataset with publicly available human single-cell RNA-seq data, we have also uncovered significant differences between human and monkey. We showed different expression patterns for *ACE2* in the lung, where the highest levels were detected in ciliated cells in monkey and pulmonary alveolar type 2 cells in human. Similarly, we observed marked differences in liver, in which monkey hepatocytes displayed higher *ACE2* and a larger number of positive cells compared to the human. We do not know whether these differences will affect the pathogenesis of COVID-19 between these two species. Nevertheless, this is a relevant finding considering that monkeys are a preferred model for studying the effectiveness of drug treatments and of vaccines against the impending COVID-19 pandemic.

12

351 Through correlation analysis, we identified new potential mechanisms that could facilitate
352 ACE2-mediated viral infection, including genes previously unreported in the context of SARS-
353 CoV-2 that are involved in stimulating different types of immune responses. We observed
354 high expression of *IDO2* and *ANPEP* in kidney, liver and lung. Expression of these can be
355 further induced by viral infection and have been reported to be immune modulators and/or
356 mediate viral entry (Ball et al., 2009; Delmas et al., 1992). These observations are relevant as
357 they highlight new potential therapeutic vulnerabilities in the current emergency. In this
358 respect, a number of inhibitors of ANPEP are currently being developed and could serve to
359 prevent the immune cell exhaustion often observed in many severe COVID-19 cases (Zheng
360 et al., 2020). Similarly, mesenchymal stem/stroma cells (MSC) have immunomodulatory
361 functions that are partly related to IDO2 production (Ball et al., 2009). It is tempting to
362 speculate that cell therapies based on MSC could ameliorate COVID-19 by normalizing
363 immune function and preventing cytokine storms (Wilson et al., 2015).

364 Intriguingly, in our data, we see heterogenous expression of *ACE2* within the individual cell
365 subtypes in six out of the nine monkey organs that we analyzed, which is also observed in the
366 three human organs analyzed. Interestingly, we noticed two different cell populations in the
367 kidney proximal tubule, one with higher *ACE2* expression than the other. We performed
368 single-cell ATAC-seq of this organ to understand whether this phenomenon has an epigenetic
369 basis. Analysis of open chromatin regions within the ACE2 locus revealed the enrichment of
370 STAT1, STAT3 and IRF1 binding sites. These transcription factors have important immune
371 functions and are direct targets of tissue protective and innate immune responses such as
372 interleukin-6 signaling pathway and interferons. Analysis of IL6R distribution showed broad
373 expression within different the *ACE2*^{+} organs in monkey and human. This suggests a link
374 between paracrine IL6 (e.g. secreted by stromal cells including tissue resident macrophages)
375 and enhanced *ACE2* expression across different organs. Higher and more widespread ACE2
376 expression could promote increased viral entry. This observation could be of the utmost
377 importance given recent reports describing clinical trials with Tocilizumab, a monoclonal
378 antibody used for IL6R blockade in patients with rheumatoid arthritis (Villiger et al., 2016), for
379 the treatment of COVID-19 (http://www.chictr.org.cn/showprojen.aspx?proj=49409). IL6 has
380 been related to aging and tissue damage (Mosteiro et al., 2018), and this may explain why
381 elderly individuals and those with underlying inflammatory conditions have more severe
382 reactions to SARS-CoV-2 infection (**Fig. 6**). Importantly, high IL6 levels have been detected in

383   plasma from COVID-19 patients (Wan et al., 2020). The proposed enhanced affinity of SARS-

384   CoV-2 for ACE2 compared to SARS-CoV may underlie the differences in the clinical course

385   between the two diseases (Shang et al., 2020).

386   All these observations revealed new potential mechanisms for COVID-19, opening new

387   therapeutic avenues for disease management. However, caution should be exercised when

388   making decisions before additional experimental validation becomes available.

389

390 **METHODS**

391

392 **Ethics statement**

393 This study was approved by the Institutional Review Board on Ethics Committee of BGI

394 (permit no. BGI-IRB19125).

395

396 **Collection of monkey tissues**

397 A 6-year old female cynomolgus monkey was purchased from Huazhen Laboratory Animal

398 Breeding Centre (Guangzhou, China). The monkey was anesthetized with ketamine

399 hydrochloride (10 mg/kg) and barbiturate (40 mg/kg) administration before being euthanized

400 by exsanguination. Tissues were isolated and placed on the ice-cold board for dissection.

401 Whole organs including lung, kidney, pancreas, liver, brain, thyroid, parotid gland, and aorta

402 were cut into 5-10 pieces, respectively (50-200 mg/piece). Samples were then quickly frozen

403 in liquid nitrogen and stored until nuclear extraction was performed. PBMC were isolated

404 from heparinized venous blood using a Lymphoprep^{TM} medium (STEMCELL Technologies,

405 #07851) according to standard density gradient centrifugation methods. PBMC were

406 resuspended in 90% FBS, 10% DMSO (Sigma Aldrich, #D2650) freezing media and frozen using

407 a Nalgene® Mr. Frosty® Cryo 1°C Freezing Container (Thermo Fisher Scientific, #5100-0001)

408 in a -80°C freezer for 24 hours before being transferred to liquid nitrogen for long-term

409 storage.

410

411 **Single-nucleus/cell suspension preparation**

412 We isolated nuclei as previously described (Bakken et al., 2018). Briefly, tissues were thawed,

413 minced and added to lysis buffer. Lysates were filtered and resuspended in cell resuspension

414 buffer. Frozen PBMC vials were rapidly thawed in a 37°C water bath for ~2 minutes, then

415 quenched with 10 ml 37°C pre-warmed 1X phosphate-buffered saline (PBS, Thermo

416 Fisher Scientific, #10010031) supplemented with 10% FBS. PBMCs were centrifuged at 500

417 *R.C.F.* for 5 minutes at room temperature. The supernatant was removed, and the cell

418 pellet was resuspended in 3 ml 37°C pre-warmed 1X PBS containing 0.04% bovine serum

419 albumin (BSA, Sangon Biotech, A600903), passed through a 40 µm cell strainer (Falcon,

420 #352340) and then centrifuged at 500 *R.C.F.* for 5 minutes at room temperature. Nuclei or

421   cells were resuspended with cell resuspension buffer at a concentration of 1,000 cells/μl for

422   single-cell library preparation.

423

424   **Single-nucleus/cell sequencing**

425   The DNBelab C Series Single-Cell Library Prep Set (MGI, #1000021082) was utilized as

426   previously described (Liu et al. 2019). In brief, single-nucleus/cell suspensions were used for

427   droplet generation, emulsion breakage, beads collection, reverse transcription, and cDNA

428   amplification to generate barcoded libraries. Indexed single-cell RNA-seq libraries were

429   constructed according to the manufacturer's protocol. The sequencing libraries were

430   quantified by Qubit™ ssDNA Assay Kit (Thermo Fisher Scientific, #Q10212). Single-cell ATAC-

431   seq libraries were prepared using DNBelab C4 Single-Cell ATAC-seq Library Prep Set (MGI).

432   DNA nanoballs (DNBs) were loaded into the patterned Nano arrays and sequenced on the

433   ultra-high-throughput DIPSEQ T1 sequencer using the following read length: 30 bp for read 1,

434   inclusive of 10 bp cell barcode 1, 10 bp cell barcode 2 and 10 bp unique molecular identifier

435   (UMI), 100 bp of transcript sequence for read 2, and 10 bp for sample index.

436

437   **Single-cell RNA-seq data processing**

438   Raw sequencing reads from DIPSEQ-T1 were filtered and demultiplexed using PISA (version

439   0.2) (https://github.com/shiquan/PISA). Reads were aligned to Macaca_fascicularis_5.0

440   genome using STAR (version 2.7.4a) (Dobin et al., 2013) and sorted by sambamba (version

441   0.7.0) (Tarasov et al., 2015). Cell versus gene UMI count matrix was generated with PISA.

442

443   **Cell clustering and identification of cell types**

444   Clustering analysis of the complete cynomolgus monkey tissue dataset was performed using

445   Scanpy (version 1.4) (Wolf et al., 2018) in a Python environment. Parameters used in each

446   function were manually curated to portray the optimal clustering of cells. In preprocessing,

447   cells or nuclei were filtered based on the criteria of expressing a minimum of 200 genes and

448   a gene which is expressed by a minimum of 3 cells or nuclei. Filtered data were ln (counts per

449   million (CPM)/100 + 1) transformed. 3000 highly variable genes were selected according to

450   their average expression and dispersion. The number of UMI and the percentage of

451   mitochondrial gene content were regressed out and each gene was scaled by default options.

452   Dimension reduction starts with principal component analysis (PCA), and the number of

16

453 principal components used for UMAP depends on the importance of embeddings. The
454 Louvain method is then used to detect subgroups of cells. Distinguishing differential genes
455 among clusters were ranked (Benjamini-Hochberg, Wilcoxon rank-sum test). Cell types were
456 manually and iteratively assigned based on overlap of literature, curated and statistically
457 ranked genes.

458 Each tissue dataset was portrayed using the Seurat package (version 3.1.1) (Stuart et al., 2019)
459 in R environment by default parameters for filtering, data normalization, dimensionality
460 reduction, clustering, and gene differential expression analysis. Finally, we annotated each
461 cell type by extensive literature reading and searching for the specific gene expression
462 pattern.

463

464 **Gene correlation and Gene Ontology (GO) term enrichment analysis**
465 The correlation between *ACE2* and other genes was drawn using Pearson correlation
466 coefficient (PCC) with gene expression value merged from cells of the same cell types with
467 the R package psych (version 1.9.12.31). To infer the biological function of highly correlated
468 genes (cor > 0.6 and adjusted P value < 0.001), we performed gene set enrichment analysis
469 using Metascape (https://metascape.org/gp/index.html).

470

471 **Differential gene expression analysis**
472 Differential expression analysis between proximal tubule S1 and proximal tubule S3 was
473 performed using the FindMarkers function of the Seurat package (version 3.1.1).

474

475 **Single-cell ATAC-seq data processing**
476 Raw sequencing reads from DIPSEQ-T1 were filtered and demultiplexed using PISA (version
477 0.2) (https://github.com/shiquan/PISA). Peak calling was performed using MACS2 (version
478 2.1.2) (Feng et al., 2012) with options -f BAM -B -q 0.01 –nomodel. The cell versus peak reads
479 count matrix was generated by custom script. To create a gene activity matrix, we extracted
480 gene coordinates for cynomolgus monkey from NCBI, and extended them to ±2 kb region
481 around TSS. The gene activity score matrix was calculated by custom script.

482

483 **Single-cell ATAC-seq cell clustering and cell type identification**

484 Cells with low fragments (<1000) and TSS proportion (<0.1) were removed. Then, filtered data

485 were imported into R and the dimensionality was reduced by latent semantic indexing.

486 Anchors between single-cell ATAC-seq and single-cell RNA-seq datasets were identified and

487 used to transfer cell type labels identified from the single-cell RNA-seq data. We embedded

488 the single-cell ATAC-seq and single-cell RNA-seq cells by the TransferData function of Seurat

489 (version 3.1.1).

490

491 **Transcription factor motif enrichment analysis**

492 To predict the motif footprint in peaks within the *ACE2* promoter, we extracted genome

493 sequences in the peak region with Seqkit (version 0.7.0) (Shen et al., 2016). The sequences

494 were imported into R and were matched with all *Homo sapiens* motifs form JASPAR2018 using

495 matchMotifs function in motifmatchr packages version 1.8.0 with default parameter.

496

497 **Human single-cell RNA-seq datasets**

498 All human single-cell RNA-seq data matrix were obtained from publicly available dataset as

499 described: (1) Kidney data from Stewart et al. was download from

500 https://www.kidneycellatlas.org/ (Stewart et al., 2019); (2) Lung data from Madissoon et al.

501 was download from https://www.tissuestabilitycellatlas.org/ (Madissoon et al., 2019); (3)

502 Liver data from Aizarani et al. was download from GEO at accession GSE124395 (Aizarani et

503 al., 2019).

504

505 **Code availability**

506 Computer code used for processing the single-cell RNA-seq and single-cell ATAC-seq will be

507 available upon request.

508

509 **Data availability**

510 All raw data have been deposited to CNGB Nucleotide Sequence Archive and the accession

511 number will be available upon request.

512

513 **Acknowledgements**

525

526 **Author contributions**

527 L.L., M.A.E., Y.H. and X.X. conceived the idea. L.L., L.H., Y.L., S.L., X.W. and Y.Yuan. designed

528 the experiment. L.H., Y.L., S.L., X.W., Y.Y., M.C. and C.W.W. collected the tissue samples. C.L.,

529 Z.W., Y.Yuan, Y. Yu, M.W., T.W., Y.L., C.W., Y.Z., T.T., Y.H., H.L., L.X., J.X. and M.C. performed

530 the experiments. X.W., T.P., Q.S., L.W., Z.Z., Y.L., S.Z. and S.L. performed the data analysis.

531 L.L., L.H., X.W., C.L., G.V., T.P., C.W. and Y.L. prepared the figures. P.H.M provided critical

532 review of the manuscript. M.A.E., G.V., C.W., Y.L. and L.L. wrote the manuscript with input

533 from all authors. X.X., Y.H., L.L. and M.A.E supervised the entire study. All other authors

534 contributed to the work. All authors read and approved the manuscript for submission.

535

536 **Competing interests**

537 Employees of BGI have stock holdings in BGI.

538

539 **FIGURE LEGENDS**

540

541 **Figure 1. Construction of single-cell atlas across nine tissues of a *Macaca fascicularis***

542 **monkey**

543 (**A**) Schematic representation of selected monkey tissues used in this study and description

544 of experimental pipeline for the single-cell sequencing.

545 (**B**) UMAP visualization of all single cells from the dataset colored by tissue/organ (left) and

546 number of cells from each tissue passing quality control (right).

547 (**C**) UMAP visualization of each cell type colored according to 44 clusters in the first round of

548 clustering. Cell type annotation is provided in the figure and is associated with a number

549 indicative of every cluster. n = 215,334 individual nuclei/cells.

550

551 **Figure 2. *ACE2* and *TMPRSS2* expression across 44 cell clusters in monkey**

552 (**A-B**) UMAP projection of *ACE2* (**A**) and *TMPRSS2* (**B**) expression in all single cells within our

553 dataset.

554 (**C**) UMAP projection of $ACE2^+/TMPRSS2^+$ cells.

555 (**D**) Barplot indicating the percentage of *ACE2* and *TMPRSS2* expressing cells within each cell

556 cluster.

557 (**E**) Bubble plots showing the level of expression of *TMPRSS2* and *ACE2* genes and the ratio of

558 expressing cells in the indicated cell types. The color of each bubble represents the level of

559 expression and the size indicates the proportion of expressing cells.

560

561 **Figure 3. Comparative analysis of *ACE2* and *TMPRSS2* expression between monkey and**

562 **human**

563 (**A-C**) UMAP projection of *ACE2* (top) and *TMPRSS2* (bottom) expression in single cells of

564 monkey lung (**A**), kidney (**B**) and liver tissues (**C**). The red arrow in this panel indicates

565 cholangiocytes. The color of the cells reflects the expression level as indicated in the scale

566 bar. (**D-F**) Bubble plots showing the ratio and expression of *ACE2 and TMPRSS2* in the

567 indicated cell types of lung (**D**), kidney (**E**) and liver (**F**) in monkey and human. The color of

568 each bubble represents the level of expression and the size indicates the proportion of

569 expressing cells.

570

Figure 4. Co-expression analysis of *ACE2*

(**A**) Volcano plot of correlation coefficients (Pearson r^2) from association tests between *ACE2* and other individual genes. The correlation coefficient for every gene (x-axis) versus the adjusted *P*-value (using Benjamini-Hochberg correction; y-axis). The genes indicated in the plot are those with a correlation score > 0.6 and an adjusted *P*-value < 0.001.

(**B**) Gene ontology analysis of genes that show high expression correlation with *ACE2*.

(**C**) Scatter plots showing the association between *ACE2* and the indicated genes. The correlation coefficients (Pearson r^2) and adjusted *P*-values are shown in the plots.

(**D**) UMAP projection of expression of the indicated genes in all single cells.

Figure 5. Chromatin accessibility analysis reveals epigenetic regulation of *ACE2* in kidney

(**A**) Schematic of experimental design for single-cell ATAC-seq of monkey.

(**B**) Joint UMAP visualization of kidney single-cell ATAC-seq data with single-cell RNA-seq data.

(**C**) UMAP visualization of single-cell ATAC-seq data.

(**D**) IGV visualization of aggregate single-cell ATAC-seq signal in each cell type.

(**E**) Ratio of ACE^+ cells in each cell type of kidney.

(**F**) The transcription factor motifs predicted based on DNA sequence within those regions of the *ACE2* locus.

(**G-H**) UMAP projection of IL6R expression and cells with $IL6R^+/ACE2^+$ cells in all kidney single cell in monkey (**G**) and human (**H**).

Figure 6. Proposed molecular mechanism for SARS-Cov-2 pathogenesis through reinforced IL6-mediated immune response in monkey and humans.

Schematic representation of potential mechanism of SARS-CoV-2 spreading through lung, kidney and liver. Kidney proximal tubule cells within the nephron have the highest expression of ACE2 receptor which facilitates virus entry. After virus contact, IL6R stimulates an immune response that, through the activation of STATs factors, potentiates the paracrine positive feedback loop that facilitates virus spreading. IL6 expression, which is higher in elderly patients and those with inflammatory conditions, is effectively targeted by anti-IL6R monoclonal antibodies leading to a more favourable disease course.

SUPPLEMENTAL FIGURE LEGENDS

Supplemental Figure 1. Quality control of the single-cell RNA-seq libraries

(**A**) Violin plot showing the number of unique molecular identifiers (UMIs) identified in each tissue.

(**B**) Violin plot showing the number of genes identified in each organ. (**C**) Heatmap showing the expression of marker genes of the indicated cell type

Supplemental Figure 2. Various cell types identified in each tissue

(**A-I**) UMAP visualization of cell clusters in lung (**A**), kidney (**B**), liver (**C**), PBMC (**D**), neocortex (**E**), parotid (**F**), aorta (**G**), thyroid (**H**) and pancreas (**I**). The name of the population corresponding to each cell cluster is indicated in every plot.

Supplemental Figure 3. *ACE2* and *TMPRSS2* expression in each tissue

(**A-B**) UMAP Projection of *ACE2* (**A**) and *TMPRSS2* (**B**) expression in each tissue.

Supplemental Figure 4. Specific accessible chromatin in each cluster of kidney

(**A**) UMAP visualization of single cells from the kidney tissue, colored by cell types.

(**B**) Volcano plot showing the differentially expressed genes between proximal tubule S1 and proximal tubule S3 cells. Examples of highly variable genes are indicated.

(**C**) UMAP projection of expression for the indicated genes in all single cells.

(**D**) The structure and specific gene expression in kidney tubules. The specific genes and *ACE2* expression level for proximal tubule S1 and proximal tubule S3 cells are indicated.

Supplemental Figure 5. Accessible chromatin analysis in each cluster of kidney

(**A**) Number of fragments captured in all cells of the two single-cell ATAC-seq libraries.

(**B**) Proportion of TSS fragments in all cells of the two single-cell ATAC-seq libraries.

(**C**) IGV visualization of specific accessible chromatin in each cell type.

(**D**) UMAP projection of *ACE2* expression in human kidney.

REFERENCES

634 **REFERENCES**

636 Aizarani, N., Saviano, A., Sagar, Mailly, L., Durand, S., Herman, J.S., Pessaux, P., Baumert, T.F.,
637 and Grun, D. (2019). A human liver cell atlas reveals heterogeneity and epithelial progenitors.
638 Nature *572*, 199-204.
639 Bakken, T.E., Hodge, R.D., Miller, J.A., Yao, Z., Nguyen, T.N., Aevermann, B., Barkan, E.,
640 Bertagnolli, D., Casper, T., Dee, N.*, et al.* (2018). Single-nucleus and single-cell transcriptomes
641 compared in matched cortical cell types. PLoS One *13*, e0209648.
642 Dobin, A., Davis, C.A., Schlesinger, F., Drenkow, J., Zaleski, C., Jha, S., Batut, P., Chaisson, M.,
643 and Gingeras, T.R. (2013). STAR: ultrafast universal RNA-seq aligner. Bioinformatics *29*, 15-21.
644 Feng, J., Liu, T., Qin, B., Zhang, Y., and Liu, X.S. (2012). Identifying ChIP-seq enrichment using
645 MACS. Nat Protoc *7*, 1728-1740.
646 Liu C, Wu T, Fan F, et al. (2019). A portable and cost-effective microfluidic system for massively
647 parallel single-cell transcriptome profiling. BioRxiv. 2019:818450.
648 Madissoon, E., Wilbrey-Clark, A., Miragaia, R.J., Saeb-Parsy, K., Mahbubani, K.T.,
649 Georgakopoulos, N., Harding, P., Polanski, K., Huang, N., Nowicki-Osuch, K.*, et al.* (2019).
650 scRNA-seq assessment of the human lung, spleen, and esophagus tissue stability after cold
651 preservation. Genome Biol *21*, 1.
652 Shen, W., Le, S., Li, Y., and Hu, F. (2016). SeqKit: A Cross-Platform and Ultrafast Toolkit for
653 FASTA/Q File Manipulation. PLoS One *11*, e0163962.
654 Stewart, B.J., Ferdinand, J.R., Young, M.D., Mitchell, T.J., Loudon, K.W., Riding, A.M., Richoz,
655 N., Frazer, G.L., Staniforth, J.U.L., Vieira Braga, F.A.*, et al.* (2019). Spatiotemporal immune
656 zonation of the human kidney. Science *365*, 1461-1466.
657 Stuart, T., Butler, A., Hoffman, P., Hafemeister, C., Papalexi, E., Mauck, W.M., 3rd, Hao, Y.,
658 Stoeckius, M., Smibert, P., and Satija, R. (2019). Comprehensive Integration of Single-Cell
659 Data. Cell *177*, 1888-1902 e1821.
660 Tarasov, A., Vilella, A.J., Cuppen, E., Nijman, I.J., and Prins, P. (2015). Sambamba: fast
661 processing of NGS alignment formats. Bioinformatics *31*, 2032-2034.
662 Wolf, F.A., Angerer, P., and Theis, F.J. (2018). SCANPY: large-scale single-cell gene expression
663 data analysis. Genome Biol *19*, 15.
664 Aizarani, N., Saviano, A., Sagar, Mailly, L., Durand, S., Herman, J.S., Pessaux, P., Baumert, T.F.,
665 and Grun, D. (2019). A human liver cell atlas reveals heterogeneity and epithelial progenitors.
666 Nature *572*, 199-204.
667 Bagheri, S.H.R., Asghari, A.M., Farhadi, M., Shamshiri, A.R., Kabir, A., Kamrava, S.K., Jalessi,
668 M., Mohebbi, A., Alizadeh, R., Honarmand, A.A.*, et al.* (2020). Coincidence of COVID-19
669 epidemic and olfactory dysfunction outbreak. medRxiv, 2020.2003.2023.20041889.
670 Bakken, T.E., Hodge, R.D., Miller, J.A., Yao, Z., Nguyen, T.N., Aevermann, B., Barkan, E.,
671 Bertagnolli, D., Casper, T., Dee, N.*, et al.* (2018). Single-nucleus and single-cell transcriptomes
672 compared in matched cortical cell types. PLoS One *13*, e0209648.
673 Ball, H.J., Yuasa, H.J., Austin, C.J., Weiser, S., and Hunt, N.H. (2009). Indoleamine 2,3-
674 dioxygenase-2; a new enzyme in the kynurenine pathway. The international journal of
675 biochemistry & cell biology *41*, 467-471.
676 Bao, L., Deng, W., Gao, H., Xiao, C., Liu, J., Xue, J., Lv, Q., Liu, J., Yu, P., Xu, Y.*, et al.* (2020).
677 Reinfection could not occur in SARS-CoV-2 infected rhesus macaques. bioRxiv,
678 2020.2003.2013.990226.

679 Chan, J.F., Yuan, S., Kok, K.H., To, K.K., Chu, H., Yang, J., Xing, F., Liu, J., Yip, C.C., Poon, R.W.*,
680 et al.* (2020). A familial cluster of pneumonia associated with the 2019 novel coronavirus
681 indicating person-to-person transmission: a study of a family cluster. Lancet *395*, 514-523.

682 Chu, P.L., Gigliotti, J.C., Cechova, S., Bodonyi-Kovacs, G., Chan, F., Ralph, D.L., Howell, N.,
683 Kalantari, K., Klibanov, A.L., Carey, R.M.*, et al.* (2017). Renal Collectrin Protects against Salt-
684 Sensitive Hypertension and Is Downregulated by Angiotensin II. J Am Soc Nephrol *28*, 1826-
685 1837.

686 Conti, P., Ronconi, G., Caraffa, A., Gallenga, C.E., Ross, R., Frydas, I., and Kritas, S.K. (2020).
687 Induction of pro-inflammatory cytokines (IL-1 and IL-6) and lung inflammation by
688 Coronavirus-19 (COVI-19 or SARS-CoV-2): anti-inflammatory strategies. J Biol Regul Homeost
689 Agents *34*.

690 Cui, J., Li, F., and Shi, Z.L. (2019). Origin and evolution of pathogenic coronaviruses. Nat Rev
691 Microbiol *17*, 181-192.

692 Delmas, B., Gelfi, J., L'Haridon, R., Vogel, L.K., Sjostrom, H., Noren, O., and Laude, H. (1992).
693 Aminopeptidase N is a major receptor for the entero-pathogenic coronavirus TGEV. Nature
694 *357*, 417-420.

695 Dobin, A., Davis, C.A., Schlesinger, F., Drenkow, J., Zaleski, C., Jha, S., Batut, P., Chaisson, M.,
696 and Gingeras, T.R. (2013). STAR: ultrafast universal RNA-seq aligner. Bioinformatics *29*, 15-21.

697 Feng, J., Liu, T., Qin, B., Zhang, Y., and Liu, X.S. (2012). Identifying ChIP-seq enrichment using
698 MACS. Nat Protoc *7*, 1728-1740.

699 Guo, Y.R., Cao, Q.D., Hong, Z.S., Tan, Y.Y., Chen, S.D., Jin, H.J., Tan, K.S., Wang, D.Y., and Yan,
700 Y. (2020). The origin, transmission and clinical therapies on coronavirus disease 2019 (COVID-
701 19) outbreak - an update on the status. Mil Med Res *7*, 11.

702 Hamm, H., Fabel, H., and Bartsch, W. (1992). The surfactant system of the adult lung:
703 physiology and clinical perspectives. Clin Investig *70*, 637-657.

704 Hamming, I., Timens, W., Bulthuis, M.L., Lely, A.T., Navis, G., and van Goor, H. (2004). Tissue
705 distribution of ACE2 protein, the functional receptor for SARS coronavirus. A first step in
706 understanding SARS pathogenesis. J Pathol *203*, 631-637.

707 Han, X., Wang, R., Zhou, Y., Fei, L., Sun, H., Lai, S., Saadatpour, A., Zhou, Z., Chen, H., Ye, F.*, et
708 al.* (2018). Mapping the Mouse Cell Atlas by Microwell-Seq. Cell *172*, 1091-1107 e1017.

709 Han, X., Zhou, Z., Fei, L., Sun, H., Wang, R., Chen, Y., Chen, H., Wang, J., Tang, H., Ge, W.*, et al.*
710 (2020). Construction of a human cell landscape at single-cell level. Nature.

711 Heinrich, P.C., Castell, J.V., and Andus, T. (1990). Interleukin-6 and the acute phase response.
712 The Biochemical journal *265*, 621-636.

713 Hoffmann, M., Kleine-Weber, H., Schroeder, S., Kruger, N., Herrler, T., Erichsen, S., Schiergens,
714 T.S., Herrler, G., Wu, N.H., Nitsche, A.*, et al.* (2020). SARS-CoV-2 Cell Entry Depends on ACE2
715 and TMPRSS2 and Is Blocked by a Clinically Proven Protease Inhibitor. Cell.

716 Jia, H.P., Look, D.C., Shi, L., Hickey, M., Pewe, L., Netland, J., Farzan, M., Wohlford-Lenane, C.,
717 Perlman, S., and McCray, P.B., Jr. (2005). ACE2 receptor expression and severe acute
718 respiratory syndrome coronavirus infection depend on differentiation of human airway
719 epithelia. J Virol *79*, 14614-14621.

720 Kim, T.S., Heinlein, C., Hackman, R.C., and Nelson, P.S. (2006). Phenotypic analysis of mice
721 lacking the Tmprss2-encoded protease. Mol Cell Biol *26*, 965-975.

722 Kock, R.A., Begovoeva, M., Ansumana, R., and Suluku, R. (2019). Searching for the source of
723 Ebola: the elusive factors driving its spillover into humans during the West African outbreak
724 of 2013-2016. Rev Sci Tech *38*, 113-122.

725 Lau, S.K., Woo, P.C., Li, K.S., Huang, Y., Tsoi, H.W., Wong, B.H., Wong, S.S., Leung, S.Y., Chan,
726 K.H., and Yuen, K.Y. (2005). Severe acute respiratory syndrome coronavirus-like virus in
727 Chinese horseshoe bats. Proc Natl Acad Sci U S A *102*, 14040-14045.
728 Lee, J.W., Chou, C.L., and Knepper, M.A. (2015). Deep Sequencing in Microdissected Renal
729 Tubules Identifies Nephron Segment-Specific Transcriptomes. J Am Soc Nephrol *26*, 2669-
730 2677.
731 Lepiller, Q., Soulier, E., Li, Q., Lambotin, M., Barths, J., Fuchs, D., Stoll-Keller, F., Liang, T.J., and
732 Barth, H. (2015). Antiviral and Immunoregulatory Effects of Indoleamine-2,3-Dioxygenase in
733 Hepatitis C Virus Infection. J Innate Immun *7*, 530-544.
734 Li, Z., Wu, M., Yao, J., Guo, J., Liao, X., Song, S., Li, J., Duan, G., Zhou, Y., Wu, X.*, et al.* (2020).
735 Caution on Kidney Dysfunctions of COVID-19 Patients. medRxiv, 2020.2002.2008.20021212.
736 Liu, C., Wu, T., Fan, F., Liu, Y., Wu, L., Junkin, M., Wang, Z., Yu, Y., Wang, W., Wei, W.*, et al.*
737 (2019). A portable and cost-effective microfluidic system for massively parallel single-cell
738 transcriptome profiling. bioRxiv, 818450.
739 Madissoon, E., Wilbrey-Clark, A., Miragaia, R.J., Saeb-Parsy, K., Mahbubani, K.T.,
740 Georgakopoulos, N., Harding, P., Polanski, K., Huang, N., Nowicki-Osuch, K.*, et al.* (2019).
741 scRNA-seq assessment of the human lung, spleen, and esophagus tissue stability after cold
742 preservation. Genome Biol *21*, 1.
743 Mason, R.J., and Williams, M.C. (1977). Type II alveolar cell. Defender of the alveolus. Am Rev
744 Respir Dis *115*, 81-91.
745 Mosteiro, L., Pantoja, C., de Martino, A., and Serrano, M. (2018). Senescence promotes in vivo
746 reprogramming through p16(INK)(4a) and IL-6. Aging Cell *17*.
747 Naicker, S., Yang, C.W., Hwang, S.J., Liu, B.C., Chen, J.H., and Jha, V. (2020). The Novel
748 Coronavirus 2019 epidemic and kidneys. Kidney Int.
749 Ong, J., Young, B.E., and Ong, S. (2020). COVID-19 in gastroenterology: a clinical perspective.
750 Gut, Epub ahead of print.
751 Peiris, J.S., Lai, S.T., Poon, L.L., Guan, Y., Yam, L.Y., Lim, W., Nicholls, J., Yee, W.K., Yan, W.W.,
752 Cheung, M.T.*, et al.* (2003). Coronavirus as a possible cause of severe acute respiratory
753 syndrome. Lancet *361*, 1319-1325.
754 Reusken, C.B., Haagmans, B.L., Muller, M.A., Gutierrez, C., Godeke, G.J., Meyer, B., Muth, D.,
755 Raj, V.S., Smits-De Vries, L., Corman, V.M.*, et al.* (2013). Middle East respiratory syndrome
756 coronavirus neutralising serum antibodies in dromedary camels: a comparative serological
757 study. Lancet Infect Dis *13*, 859-866.
758 Rothe, C., Schunk, M., Sothmann, P., Bretzel, G., Froeschl, G., Wallrauch, C., Zimmer, T., Thiel,
759 V., Janke, C., Guggemos, W.*, et al.* (2020). Transmission of 2019-nCoV Infection from an
760 Asymptomatic Contact in Germany. The New England journal of medicine *382*, 970-971.
761 Santer, R., and Calado, J. (2010). Familial renal glucosuria and SGLT2: from a mendelian trait
762 to a therapeutic target. Clin J Am Soc Nephrol *5*, 133-141.
763 Shang, J., Ye, G., Shi, K., Wan, Y., Luo, C., Aihara, H., Geng, Q., Auerbach, A., and Li, F. (2020).
764 Structural basis of receptor recognition by SARS-CoV-2. Nature.
765 Shen, W., Le, S., Li, Y., and Hu, F. (2016). SeqKit: A Cross-Platform and Ultrafast Toolkit for
766 FASTA/Q File Manipulation. PLoS One *11*, e0163962.
767 Sigdel, T.K., Shoemaker, L.D., Chen, R., Li, L., Butte, A.J., Sarwal, M.M., and Steinberg, G.K.
768 (2013). Immune response profiling identifies autoantibodies specific to Moyamoya patients.
769 Orphanet journal of rare diseases *8*, 45.

770 Stewart, B.J., Ferdinand, J.R., Young, M.D., Mitchell, T.J., Loudon, K.W., Riding, A.M., Richoz,
771 N., Frazer, G.L., Staniforth, J.U.L., Vieira Braga, F.A.*, et al.* (2019). Spatiotemporal immune
772 zonation of the human kidney. Science *365*, 1461-1466.
773 Stuart, T., Butler, A., Hoffman, P., Hafemeister, C., Papalexi, E., Mauck, W.M., 3rd, Hao, Y.,
774 Stoeckius, M., Smibert, P., and Satija, R. (2019). Comprehensive Integration of Single-Cell
775 Data. Cell *177*, 1888-1902 e1821.
776 Su, S., Wong, G., Shi, W., Liu, J., Lai, A.C.K., Zhou, J., Liu, W., Bi, Y., and Gao, G.F. (2016).
777 Epidemiology, Genetic Recombination, and Pathogenesis of Coronaviruses. Trends Microbiol
778 *24*, 490-502.
779 Tarasov, A., Vilella, A.J., Cuppen, E., Nijman, I.J., and Prins, P. (2015). Sambamba: fast
780 processing of NGS alignment formats. Bioinformatics *31*, 2032-2034.
781 Turner, A.J., Hiscox, J.A., and Hooper, N.M. (2004). ACE2: from vasopeptidase to SARS virus
782 receptor. Trends Pharmacol Sci *25*, 291-294.
783 Villiger, P.M., Adler, S., Kuchen, S., Wermelinger, F., Dan, D., Fiege, V., Butikofer, L., Seitz, M.,
784 and Reichenbach, S. (2016). Tocilizumab for induction and maintenance of remission in giant
785 cell arteritis: a phase 2, randomised, double-blind, placebo-controlled trial. Lancet *387*, 1921-
786 1927.
787 Walls, A.C., Park, Y.J., Tortorici, M.A., Wall, A., McGuire, A.T., and Veesler, D. (2020). Structure,
788 Function, and Antigenicity of the SARS-CoV-2 Spike Glycoprotein. Cell, Epub ahead of print.
789 Wan, S., Yi, Q., Fan, S., Lv, J., Zhang, X., Guo, L., Lang, C., Xiao, Q., Xiao, K., Yi, Z.*, et al.* (2020).
790 Characteristics of lymphocyte subsets and cytokines in peripheral blood of 123 hospitalized
791 patients with 2019 novel coronavirus pneumonia (NCP). medRxiv, 2020.2002.2010.20021832.
792 Wentworth, D.E., and Holmes, K.V. (2001). Molecular determinants of species specificity in
793 the coronavirus receptor aminopeptidase N (CD13): influence of N-linked glycosylation. J Virol
794 *75*, 9741-9752.
795 Wilson, J.G., Liu, K.D., Zhuo, H., Caballero, L., McMillan, M., Fang, X., Cosgrove, K., Vojnik, R.,
796 Calfee, C.S., Lee, J.W.*, et al.* (2015). Mesenchymal stem (stromal) cells for treatment of ARDS:
797 a phase 1 clinical trial. Lancet Respir Med *3*, 24-32.
798 Wolf, F.A., Angerer, P., and Theis, F.J. (2018). SCANPY: large-scale single-cell gene expression
799 data analysis. Genome Biol *19*, 15.
800 Yu, L., Lv, J.C., Zhou, X.J., Zhu, L., Hou, P., and Zhang, H. (2011). Abnormal expression and
801 dysfunction of novel SGLT2 mutations identified in familial renal glucosuria patients. Hum
802 Genet *129*, 335-344.
803 Zheng, M., Gao, Y., Wang, G., Song, G., Liu, S., Sun, D., Xu, Y., and Tian, Z. (2020). Functional
804 exhaustion of antiviral lymphocytes in COVID-19 patients. Cell Mol Immunol, Epub ahead of
805 print.
806 Zhu, N., Zhang, D., Wang, W., Li, X., Yang, B., Song, J., Zhao, X., Huang, B., Shi, W., Lu, R.*, et al.*
807 (2020). A Novel Coronavirus from Patients with Pneumonia in China, 2019. The New England
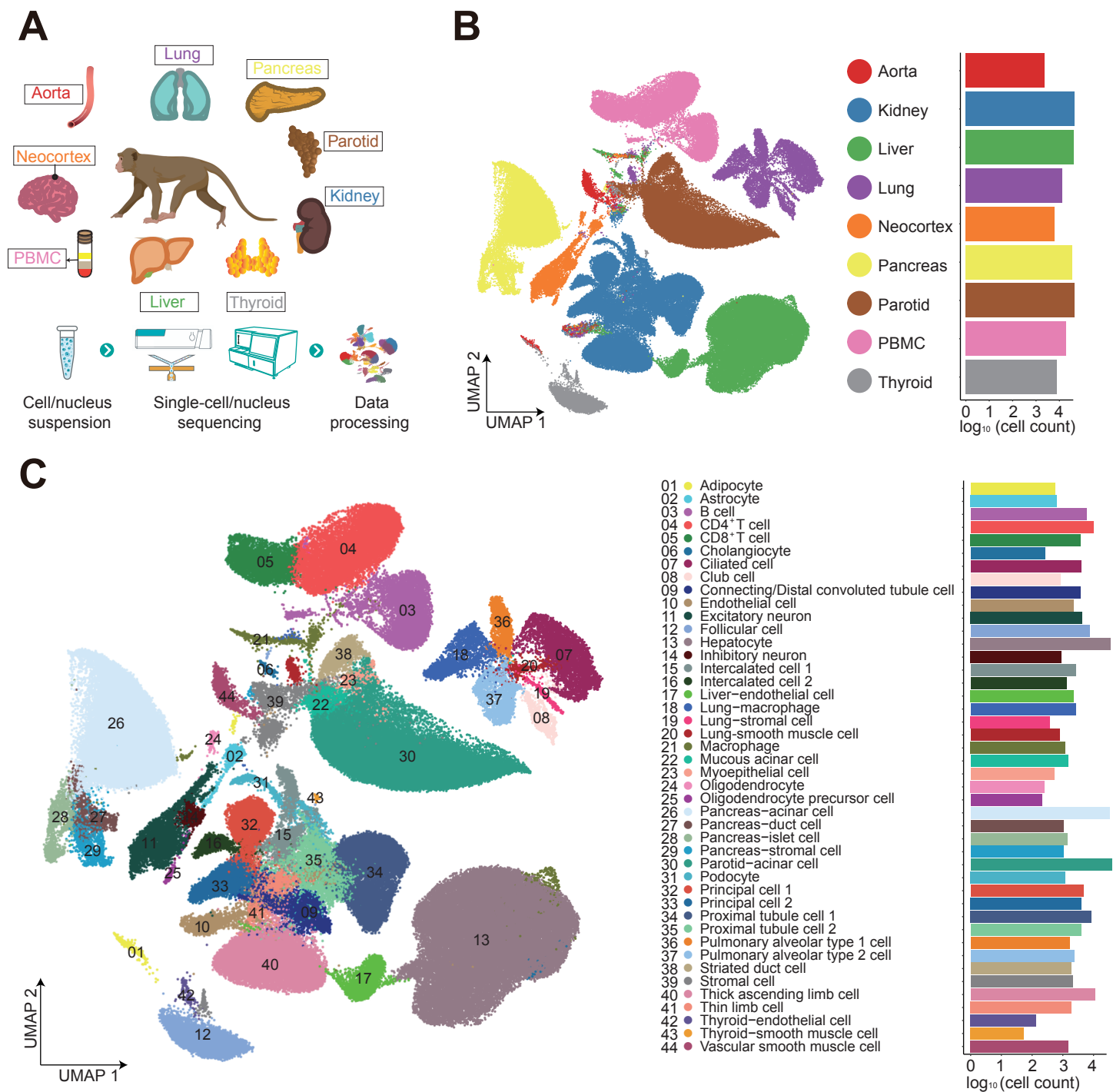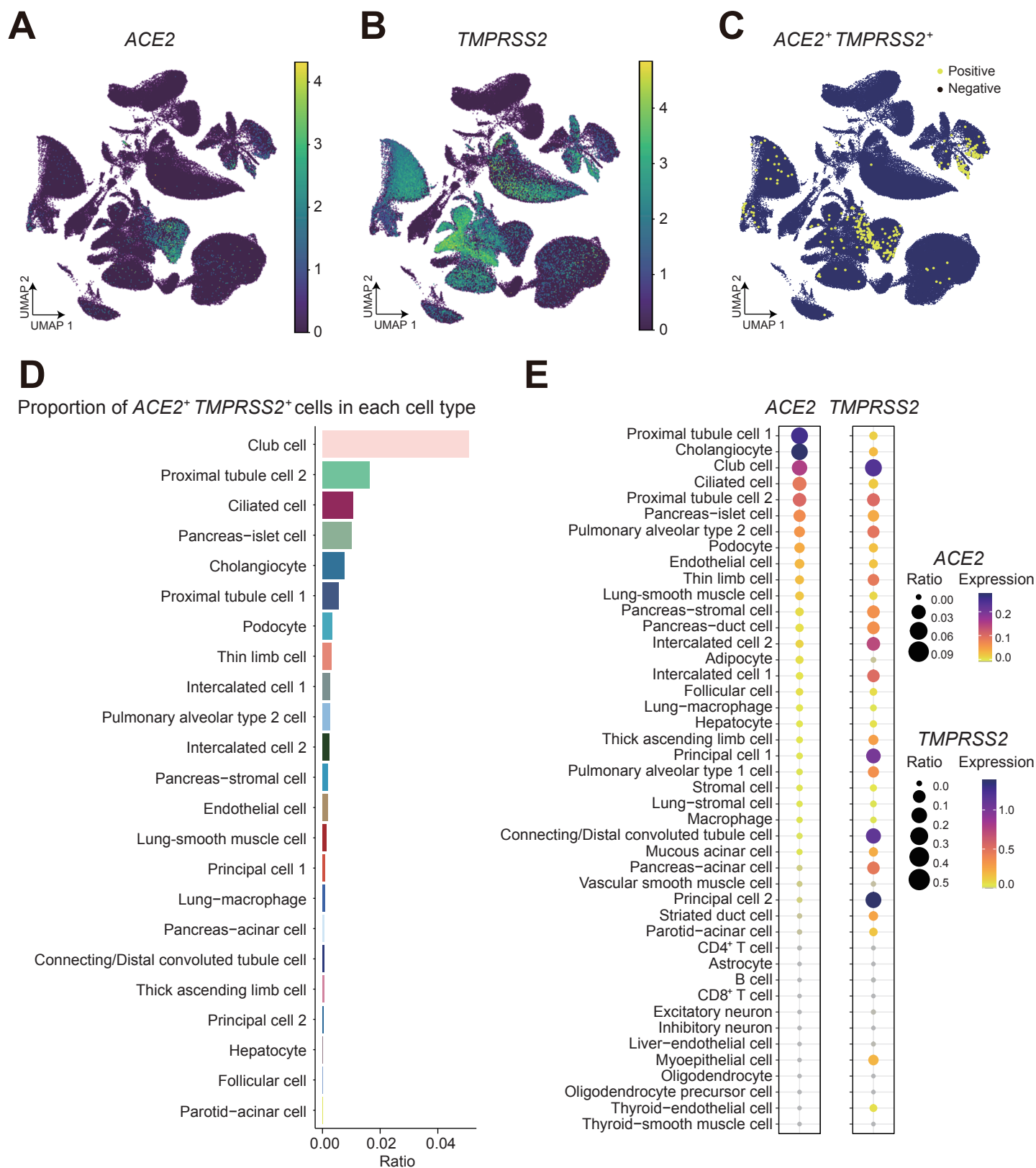808 journal of medicine *382*, 727-733.
809

A
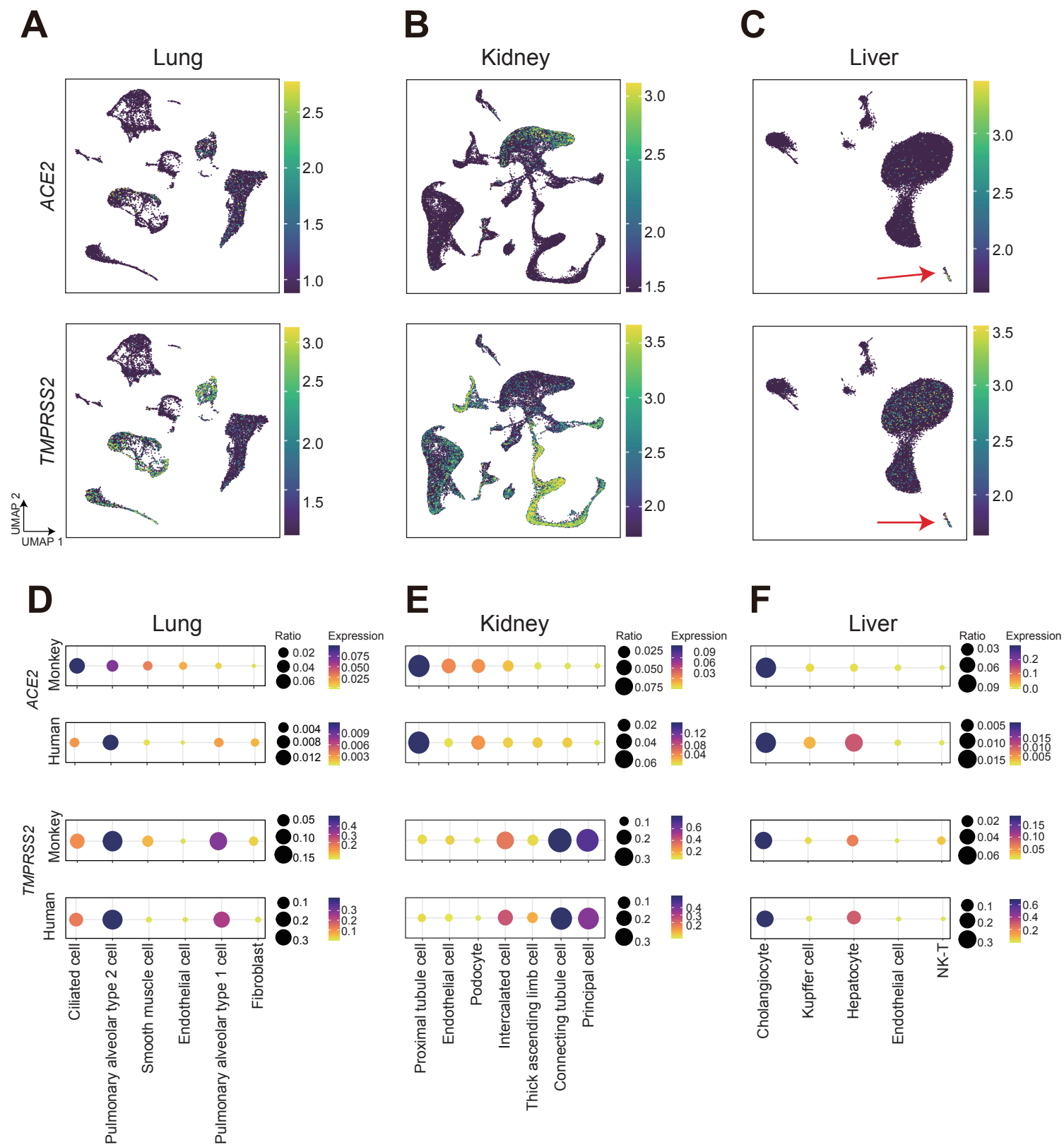
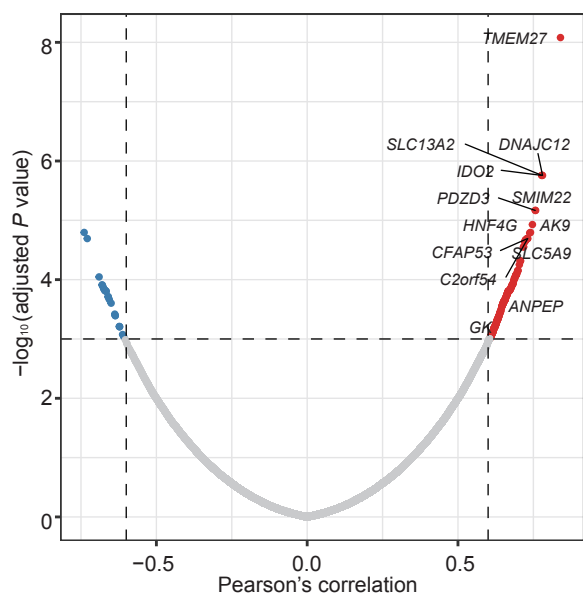Aorta
Lung
Pancreas
Neocortex
Parotid
Kidney
PBMC
Liver
Thyroid

Cell/nucleus suspension → Single-cell/nucleus sequencing → Data processing

B

UMAP 2
UMAP 1

- Aorta
- Kidney
- Liver
- Lung
- Neocortex
- Pancreas
- Parotid
- PBMC
- Thyroid

$\log_{10}$ (cell count)

C

UMAP 2
UMAP 1

01 Adipocyte
02 Astrocyte
03 B cell
04 CD4$^+$ T cell
05 CD8$^+$ T cell
06 Cholangiocyte
07 Ciliated cell
08 Club cell
09 Connecting/Distal convoluted tubule cell
10 Endothelial cell
11 Excitatory neuron
12 Follicular cell
13 Hepatocyte
14 Inhibitory neuron
15 Intercalated cell 1
16 Intercalated cell 2
17 Liver−endothelial cell
18 Lung−macrophage
19 Lung−stromal cell
20 Lung-smooth muscle cell
21 Macrophage
22 Mucous acinar cell
23 Myoepithelial cell
24 Oligodendrocyte
25 Oligodendrocyte precursor cell
26 Pancreas−acinar cell
27 Pancreas−duct cell
28 Pancreas−islet cell
29 Pancreas−stromal cell
30 Parotid−acinar cell
31 Podocyte
32 Principal cell 1
33 Principal cell 2
34 Proximal tubule cell 1
35 Proximal tubule cell 2
36 Pulmonary alveolar type 1 cell
37 Pulmonary alveolar type 2 cell
38 Striated duct cell
39 Stromal cell
40 Thick ascending limb cell
41 Thin limb cell
42 Thyroid−endothelial cell
43 Thyroid−smooth muscle cell
44 Vascular smooth muscle cell

$\log_{10}$ (cell count)

Figure 1

Figure 2

Figure 3

Figure 4

A

Tn5 transposed single-nuclei → Single nucleus barcoding → Sequencing → Data processing

B

Joint scATAC and scRNA visualization

scATAC-seq
scRNA-seq

UMAP 2
UMAP 1

C

scATAC-seq

Thick ascending limb cell
Podocyte
Stromal cell
Thin limb cell
Endothelial cell
Proximal tubule S1
Distal convoluted tubule cell
Proximal tubule S3
Intercalated cell
Connecting tubule cell
Principal cell

E

Ratio of *ACE2*⁺ cells in each cell type

Ratio

Proximal tubule S3
Proximal tubule S1
Thin limb cell
Thick ascending limb cell
Principal cell
Podocyte
Stromal cell
Intercalated cell
Endothelial cell
Distal convoluted tubule cell
Connecting tubule cell

D

Aggregated scATAC-seq

Connecting tubule cell
Distal convoluted tubule cell
Endothelial cell
Intercalated cell
Stromal cell
Podocyte
Principal cell
Thick ascending limb cell
Thin limb cell
Proximal tubule S1
Proximal tubule S3

ACE2

F

IRF1   STAT1   STAT3

G

IL6R   *ACE2*⁺ *IL6R*⁺

Monkey

Positive
Negative

H

Human

Positive
Negative

UMAP 2
UMAP 1

Figure 5

Figure 6

Supplemental Figure 1

A Lung

B Kidney

C Liver

D PBMC

E Neocortex

F Parotid

G Aorta

H Thyroid

I Pancreas

Supplemental Figure 2

A *ACE2*   **B** *TMPRSS2*

Pancreas

Parotid

PBMC

Thyroid

Aorta

Neocortex

UMAP 2
UMAP 1

Supplemental Figure 3

A scRNA-seq

Podocyte

Proximal tubule S3

Proximal tubule S1

Distal convoluted tubule cell

Stromal cell   Intercalated cell

Endothelial cell

Connecting tubule cell

Thick ascending limb cell

Thin limb cell

Principal cell

UMAP 2

UMAP 1

B

$-\log_{10}$(adjusted P value)

$\log_2$(fold change)

SLC7A13

SLC5A2

ACE2

C

SLC5A2

SLC7A13

D

Proximal tubule S1
(*SLC5A2*[+]/*ACE2* Low)

Proximal tubule S3
(*SLC7A13*[+]/*ACE2* High)

Supplemental Figure 4

Supplemental Figure 5